Article

Journal of the Brazilian Chemical Society

https://dx.doi.org/10.21577/0103-5053.20240054

J. Braz. Chem. Soc. **2024**, *35*, 11, e-20240054, 1-15

Pure and Cobalt-Modified ZnO Nanostructures Prepared by a New Synthesis Route Applied to Environmental Remediation

Eryka T. D. Nobrega,[a] Kelvin C. de Araújo,[a] Ailton J. Moreira,[b] Regiane C. de Oliveira,[a] Gelson T. S. T. da Silva,[a] Sirlon F. Blaskievicz,[a] Leandro L. Soares,[a] Sherlan G. Lemos,[c] Lucia H. Mascaro[a] and Ernesto C. Pereira[a,]*

[a]*Departamento de Química, Universidade Federal de São Carlos, 13565-905 São Carlos-SP, Brazil*

[b]*Instituto de Química, Universidade do Estado de São Paulo (UNESP), 14800-060 Araraquara-SP, Brazil*

[c]*Departamento de Química, Universidade Federal da Paraíba, 58051-970 João Pessoa-PB, Brazil*

Pure and cobalt-doped 3D ZnO were produced using the microwave (MW)-ultraviolet (UV)-visible (Vis) radiation-assisted hydrothermal method (MW-UV-Vis HM). Using experimental design, the effects of cobalt and UV-Vis radiation during the synthesis stage on the physicochemical properties of the materials were evaluated with different characterization techniques such as X-ray diffraction, scanning and transmission electron microscopy, diffuse reflectance, and electrochemistry. The presence of cobalt had a great influence on the reduction of charge donors in the ZnO matrix and had their photocatalytic properties improved when produced under the effect of UV-Vis radiation. The catalytic activity of the materials has been verified in important environmental remediation reactions, such as the electrochemical reduction of CO_2 and the photocatalytic degradation of emerging pollutants. The results achieved in this study show competitive efficiency values for CO_2 reduction (97%) and photocatalytic degradation (91%) of emerging pollutants in natural waters, illustrating the great versatility of the produced material in distinct applications.

Keywords: microwave synthesis, photocatalysis, CO_2 reduction, emerging pollutants, environmental remediation, chemometrics

Introduction

The development and use of semiconductors have been consolidated worldwide due to their variety of technological applications. These materials have been studied as sensors,[1] antibacterial agents,[2,3] energy converters,[4] magnetic materials,[5,6] chemical speciation,[7,8] and environmental remediation.[9] This latest application has been recognized due to the numerous pollution problems resulting from the presence of emerging contaminants in ecosystems.[10] Heterogeneous photocatalysis is a widely investigated process for the degradation of emerging pollutants and the use of ZnO-based semiconductors has shown excellent results for this environmental application.[10-12] Zinc oxide (ZnO) despite being a well-known semiconductor for decades, still has great potential for photocatalytic applications, especially when obtained as 3D structures.[13,14] For instance, the hexagonal wurtzite structure can be easily produced using different synthesis methods, and precise control of the synthesis variables enables the production of 3D structures with improved photocatalytic activity.[15] However, ZnO is a high-gap semiconductor, requiring an energy of around 3.2 eV to promote the electron from the valence band (VB) to the conduction band (CB).[7] This conditions the use of ZnO in photocatalytic systems operated under ultraviolet radiation. On the other hand, ZnO can undergo chemical or structural modifications to improve its physicochemical properties and transform it into a semiconductor capable of absorbing light across a broad range of the electromagnetic spectrum.

The Co^{2+} ion is a chemical species that has the potential to extend the light absorption range of semiconductors.[16,17] Its ionic radius (0.072 nm) is close to the ionic radius of Zn^{2+} (0.074 nm), which facilitates the direct substitution of these species by Co^{2+} in the crystal lattice of ceramic matrices.[18]

*e-mail: ernesto@ufscar.br
Editor handled this article: Célia M. Ronconi (Associate)

When ZnO matrices are modified with Co^{2+}, electronic transfers between the ZnO band and the d-electrons of the Co^{2+} ions can optimize the photocatalytic properties of this material.[19] Pure or doped ZnO is obtained by different synthesis methods,[20] but the search for obtaining 3D structures through fast and more energetic routes can contribute to the production of new materials.[15] In a recent publication,[13] microwave-assisted hydrothermal method (MHM) was successfully used to produce high controlled 3D ZnO materials with high photocatalytic performance. Additionally, a synthesis method assisted by microwave-ultraviolet-visible radiation (MW-UV-Vis) has shown efficiency in obtaining TiO_2 doped with samarium.[21]

The microwave hydrothermal method is widely recognized for producing materials with high crystallinity, reduced particle size and high efficiency in the incorporation of dopants into ceramic structures.[22] When a second radiation source is added to this synthesis process, the crystal structures produced can have their physicochemical properties changed due to the action of this additional energy.[21] In this scenario, the surface energies at the grain boundary are altered, promoting the formation of different oxidation states of the metal precursors. As a result of these changes, semiconductors can be formed with a high number of structural defects that are important for improving the photocatalytic properties of materials used in environmental remediation.[23] Currently, the scientific community has focused its efforts on applying semiconductors in individual reactions, seeking to exploit oxidation or reduction reactions of photocatalysts. However, it is important to note that a photocatalyst that performs well in oxidation reactions may also be efficient in reduction reactions. Therefore, investigating the obtaining of Co-doped 3D ZnO using MW-UV-Vis HM can bring new insights. The semiconductors produced by this method could be effective for a range of catalytic applications, including environmental remediation and CO_2 sequestration,[24,25] which are currently in high demand.

In electrochemical CO_2 reduction systems, the Co^{2+} ion has shown some interesting properties for the process, such as stability, good selectivity for CO and high faradaic efficiency.[26] The incorporation of Co^{2+} into 3D hierarchical structures has also been found to be effective for CO_2 conversion reactions due to the combination of the structural, morphological and optical characteristics of these materials with the ability of cobalt to form Co^{2+} and Co^{3+} species,[27] which optimizes charge transfer processes in electrochemical reactions.[28] These properties can also be considered in the photocatalytic degradation of emerging contaminants present in different ecosystems around the world.[29,30] However, important conditions associated with this type of application must be observed to consider its feasibility for implementation.

The literature[31] shows that some photocatalysts are effective in remediating one class of organic pollutants, but not others. This suggests that investigating various molecules during the application stage is essential.[31] Mixtures of pollutants based on real matrices, such as surface water or sewage, are more complex to treat than effluents prepared in ultrapure water and made up of simple composition.[32] This difficulty is due to the natural competition that different compounds present in the mixture exert on the degradation process and, therefore, an in-depth knowledge of photocatalytic degradation mechanisms is required. An additional difficulty in heterogeneous photocatalysis research is monitoring and quantifying the degraded compounds. This is because chromatography, the standard technique in such studies, is costly and can be of limited use.[33] As an alternative, the use of higher-order calibration has proven to be an efficient, simple, and environmentally friendly approach to monitoring these compounds in complex environmental matrices. Using equipment such as spectrofluorometers or UV-Vis spectrophotometers to obtain excitation emission matrices (EEM) and molecular absorption spectra, respectively, in association with methodologies such as multivariate curve resolution (MCR) or parallel factor analysis (PARAFAC), qualitative and quantitative analyses are successfully achieved to monitor these compounds in different matrices.[34-36]

In this sense, this study aims to obtaining cobalt-doped 3D ZnO using MW-UV-Vis HM, which to our knowledge has no reports in the literature. This approach could open new opportunities to explore the influence of UV-Vis radiation on the growth mechanism of crystalline structures and thus achieve better photocatalyst performances for various technological applications. Furthermore, the use of higher-order calibration as an analytical tool is an opportunity to expand the use of this technique as an alternative to conventional analysis methods which are considered expensive, generate high amounts of waste and are not yet widely accessible.

Experimental

Nanoparticle synthesis

The syntheses of pure and cobalt-modified 3D ZnO nanostructures were carried out using an adaptation of the protocol described in Silva *et al.*[13] The syntheses were carried out following a 2^2 full factorial design strategy that was employed to assess the effects of the utilization of the microwave discharge electrodeless cadmium lamp (MDEL,

Anton Paar brand, catalog No. = 16847) and the incorporation of cobalt on the material characteristics. This approach aims to explore, map and model the behavior of the response within a given experimental space, maximizing the information obtainable from a limited number of experimental runs, saving time and resources. Cobalt was chosen as a transition metal that can be found in two oxidation states (Co^{2+}/Co^{3+}), mobilizing d-level electrons when excited by UV-Vis light. The presence of the UV-Vis light source (MDEL) during the synthesis can result in the incorporation of Co^{2+}/Co^{3+} and formation defects in 3D ZnO crystalline lattice. The levels of each variable are related to whether MDEL or Co is used or not in the synthesis (Table S1, Supplementary Information (SI) section), where the combination of two levels with two variables totals 4 experiments. This simplified design enables an efficient analysis of the main effects and the interaction between variables. Through this approach, valuable insights into correlations between independent variables and the dependent variable can be derived, contributing to a comprehensive understanding of relationships within the context of the study. 1.32 g of zinc acetate (99%, Sigma-Aldrich, Burlington, USA) and 0.051 g of cobalt acetate dihydrate (99%, Synth, Diadema, Brazil) were solubilized in 10 mL of a 75:25 ethylene glycol (EG, 99%, Sigma-Aldrich, Burlington, USA):water mixture. These values correspond to a Co/Zn = 3% mass ratio (theoretical). In the synthesis assisted by MW-UV-Vis radiation,[21] the chemical precursors and the MDEL were added to a 75 mL polytetrafluoroethylene (PTFE) vessel. In contrast, when the synthesis was assisted only by microwave radiation, MDEL was not added to the reaction vessel. The sealed vessel was placed in a Mars6 microwave oven (CEM, 60 Hz, Matthews, USA) and submitted to microwave radiation at a fixed power of 600 W for 10 min. The synthesis parameters (temperature and power) were monitored by an infrared sensor. The synthesis system is illustrated in Figure S1 (SI section).

Characterization

Powder X-ray diffraction (XRD) analyses were performed for all samples using a D/Max-2500PC diffractometer (Rigaku, Japan) with Cu Kα radiation (λ = 0.154184 nm), angle of diffraction 2θ ranging from 10 to 110°, and a scanning step of 0.02° min^{-1} to obtain details of crystal structures. Rietveld refinement method was applied for quantitative analysis of the phase using GSAS-EXPGUI software.[37] Specific surface areas, which is a parameter important of interaction between molecule-material, were examined on a Micromeritics Gemini VII analyzer (Norcross, GA, USA), 77 K nitrogen absorption, using the Brunauer-Emmett-Teller technique (BET). The morphology and radial size distribution were characterized by field emission scanning gun electron microscopy (FEG-SEM) operated at 5 kV (Supra 35-VP, Carl Zeiss, Oberkochen, Germany). The percentage by mass of cobalt, zinc, and oxygen to pure, and Co-modified ZnO samples were evaluated using energy dispersive spectroscopy (EDS), 10,000 magnification, and 15 kV in backscattered (BSE) mode coupled to the scanning electron microscope (Hitachi, TM4000 Plus, Tokyo, Japan). Transmission electron microscopy (TEM), high-resolution transmission (HR-TEM), and selected area electron diffraction (SAED) images were obtained using an FEI TECNAI F20 microscope (FEI, Oregon, USA), operating at 200 kV. This measurement makes it possible to obtain in-depth details of the shape, crystallinity, distance between crystalline planes, and identification of the crystalline phases of ZnO.

The bandgap energy (E_g), which is an important parameter for identifying the energy required for the electronic transition process was calculated by constructing Tauc plots based on the conversion of diffuse reflectance into the rate of absorption coefficient and scattering, according to the Kubelka-Munk model.[38] For this, diffuse reflectance UV-Vis analysis was performed using a UV-Vis spectrophotometer with an integrating sphere (ISR-2600 Plus, Shimadzu, Kyoto, Japan) at the range of 200-800 nm.

To explore the flat band potential (E_{FB}) and thus calculate the approximate potential of the VB and CB of the pure samples and cobalt-modified, we applied a spin-coating technique to deposit the samples onto clean fluorine-doped tin oxide (FTO) substrates. The Mott-Schottky plot was generated in triplicate by recording electrochemical impedance in potential scan mode within the range of 0.85 to –0.15 V *vs*. reversible hydrogen electrode (RHE), using a 10 mV amplitude potential and a frequency of 1 kHz, in a 0.5 mol L^{-1} Na_2SO_4 solution with a pH of 5.5. Reference and counter electrodes were provided by an Ag/AgCl/KCl (Sigma-Aldrich, Burlington, USA) saturated electrode and a platinum wire, respectively. The initially obtained E_{FB} in Ag/AgCl was converted for potential *vs*. RHE using equation 1.[39]

$$E_{(RHE,\ pH=5.5)} = E_{Ag/AgCl} + 0.198 + (0.059 \times pH_{electrolyte}) \quad (1)$$

Electrocatalytic assays

All the materials produced were applied to electrochemical CO_2 reduction reaction (eCO_2RR) to investigate the reduction reactions in the CB. To prepare

the gas diffusion electrodes (GDE) for eCO_2RR, a catalyst ink was sprayed-deposited onto a carbon paper (Sigracet 39BB, Bonn, Germany) substrate. The ink contained 8 mg of powder, consisted of 4 mg of conductive carbon black (Vulcan XC 72, Fuel cell store, Bryan, Texas, USA) and 4 mg of prepared Zn-based catalyst, and 17 µL of ionomer (Sustainion XA-95% in ethanol, Dioxide Materials Inc., Boca Raton, Florida) added to 1 mL of a 1:1 water:isopropanol (Sigma Aldrich, Burlington, USA) mixture. The bulk loading of Zn-based catalyst on the GDE was 0.75 mg cm^{-2}. Before starting the experiments, the GDE were left to dry overnight at room temperature to prevent alcohol contamination.

eCO_2RR experiments were carried out using a potentiostat/galvanostat (Autolab PGSTAT204, Metrohm, Herisau, Switzerland). The investigations were conducted within a flow electrochemical cell (Micro Flow Cell, Electrocell, Amherst, New York, USA), with an anionic exchange membrane (AEM, FAB-PK-130, Fuel Cell Store, Bryan, Texas, USA) separating the cathode and anode sides. The electrolyte (0.5 mol L^{-1} KOH, Sigma-Aldrich, Burlington, USA) was consistently circulated within the cell at a flow rate of 6 mL min^{-1} using a peristaltic pump. Furthermore, the cathode side was purged with CO_2 gaseous (99.99%, White Martins, Brazil) at a flow rate of 30 mL min^{-1}, as determined by a Supelco manual rotameter. The working electrodes consisted of the Zn-based materials that were prepared, while the counter and reference electrodes were nickel foam and an Ag/AgCl leak-free electrode, respectively. Different applied potentials were utilized to conduct electrolysis, and the gaseous product was subjected to analysis at 30 min intervals. For gas sampling, the gaseous components discharged from the cell were conveyed into a sack via the continuous CO_2 flow. Following that, minute amounts were collected using an inert bag and inserted manually by syringe into a gas chromatograph (Agilent 8860, Santa Clara, USA), which was equipped with a flame ionization detector (FID) and a thermal conductivity detector (TCD). A Carboxen 1010 PLOT capillary column was used in the gas chromatograph, and helium was used as the carrier gas.

Photocatalytic assays

This study investigated the photocatalytic activity of the materials in relation to the formation of reactive oxygen species (ROS) in VB and CB. The degradation of emerging pollutants was used as a measure of this activity. Sertraline (SRTL, 98%, Santa Cecilia Pharmacy, Poços de Caldas, MG, Brazil), fluoxetine (FLX, 98%, Santa Cecilia Pharmacy, Poços de Caldas, MG, Brazil), ofloxacin (OFX, 99%, Vetranal, Sigma-Aldrich, Burlington, USA) and diclofenac sodium (DCF, 99%, Sigma- Aldrich, Burlington, USA), classified as emerging contaminants, were used to investigate the photoactivity of the nanomaterials. In the study of the photocatalytic degradation the emerging pollutants (STRL + FLX or OFX + DCF) in natural waters, a complete 2^2 factorial design was performed to investigate different scenarios regarding the semiconductor and its application on the photocatalysis of different mixtures of pharmaceuticals. The combination of two levels with two variables totals 4 independent experiments, which represent all possible combinations of the high and low levels for each of the variables under investigation. Through these photocatalytic degradation data, it is possible to statistically analyze the behavior of each independent variable in the photocatalytic process and by what means they interact in the removal of such pharmaceuticals from surface waters. FLX or DCF were used only as concomitants to increase the complexity of the solution under photodegradation, with SRTL and OFX selected as targets for the photocatalytic assays. Thus, the quantitative analyses were applied only to SRTL or OFX. The experiments of the design are detailed in Table S2 (SI section). Photodegradation experiments were carried out under UV-C radiation, considering all conceivable combinations listed in Table S2.

5 mg of each catalyst and 10 mL of the emerging contaminants solution (SRTL (70 µg L^{-1}) + FLX (4000 µg L^{-1}) or OFX (240 µg L^{-1}) + DCF (200 µg L^{-1})) were added to a 50 mL glass beaker and kept under stirring for 30 min to reach adsorption-desorption equilibrium. Then, the solutions were submitted to photodegradation under UV-C (254 nm, Phillips) light at different time intervals (0 to 30 min). After that, the samples were filtered using a 0.45 µm polyvinylidene difluoride (PVDF) membrane to remove the powder, and SRTL or OFX analysis was performed using a spectrofluorophotometer RF-5301pc (Shimadzu, Tokyo, Japan) to obtain the EEM. For SRTL, the spectral ranges were λ_{exc} = 240-270 nm and λ_{em} = 282-400 nm, while for OFX, it was λ_{exc} = 245-305 nm and λ_{em} = 330-465 nm. The linear ranges of the calibration curves were 100-800 µg L^{-1} for SRTL and 10-150 µg L^{-1} for OFX. Ultrapure water EEM was subtracted from sample EEM to remove Raman scattering. PARAFAC was used to decompose the spectra and separate each component of the mixture. Limits of detection (LOD) and quantification (LOQ) were estimated from the limit of blank, as described in literature.[40-42] The solutions containing the mixture of drugs were prepared using surface water collected at the Poços de Caldas Water Treatment Plant, Minas Gerais Brazil (latitude: –21.78759; longitude: –46.56137). The physicochemical characteristics of the surface water are shown in Table S3 (SI section).

Further details of the photochemical reactor used in this study can be found in the literature.[35] To investigate the degradation mechanism, the use of isopropyl alcohol (IPA, Sigma-Aldrich, Burlington, USA), silver nitrate (SN, Sigma-Aldrich, Burlington, USA), ascorbic acid (AAS, Sigma-Aldrich, Burlington, USA), and ethylenediaminetetraacetic acid (EDTA, Sigma-Aldrich, Burlington, USA) as $^{\bullet}OH$, e^-, $O_2^{\bullet-}$ and h^+ scavengers, respectively, were used following the procedure described in the literature.[43,44] Probe assays for $^{\bullet}OH$ using coumarin (99%, Sigma-Aldrich, Burlington, USA) were carried out in the photochemical system. A volume of 10 mL of a 1.5 mg L^{-1} coumarin solution was added to the beaker with different materials and irradiated under the same conditions of the OFX or SRTL degradation assays. In the presence of $^{\bullet}OH$, coumarin is converted to 7-hydroxycoumarin (7HC, umbelliferone, Sigma-Aldrich, Burlington, USA) which has an emission peak centered on 460 nm when excited at 330 nm.[45] A calibration curve based on the 7HC analytical standard was constructed by applying solutions with a concentration of 1 to 20 μg L^{-1}. The concentration of $^{\bullet}OH$ produced was calculated as described in the literature.[46]

Results and Discussion

Physicochemical properties of materials

The energy conditions of the synthesis system using MW-UV-Vis HM were shown in Figure S2a (SI section). The temperature was continuously increased to 190 ºC due to the microwave power, which was set at 600 W for the 10 min synthesis time. These conditions were adopted so that the MDEL remained in operation continuously, emitting the spectrum shown in Figure S2b with the same intensity throughout the ZnO formation stage. At 600 W, MDEL exhibited a spectrum with emission peaks ranging from 193 to 867 nm. In particular, the emission peaks in the UV region (outlined in yellow) can promote profound changes in the energetic conditions of formation of the nanometric ZnO structures. This light energy, in addition to interacting with specific facets of 3D ZnO and influencing some of its physicochemical properties, can promote the photolysis of the EG/H_2O mixture, releasing different oxidizing species into the reaction medium.[47] These processes result in the formation of ionic species with varying oxidation states, specific morphologies and point defects in the synthesized materials.

The XRD patterns of the pure and cobalt-modified ZnO synthesized with and without MDEL (Figure 1a) showed that the single-phase samples were synthesized. All peaks were indexed to the ZnO phase according to the Inorganic Crystal Structure Database (ICSD) number 1011258, with hexagonal structure, spatial group (*P63mc*), and two molecular formulas *per* unit cell (Z = 2).[48] Furthermore, cobalt-modified ZnO showed no secondary phase of cobalt or any other subproducts, confirming that the only hexagonal ZnO phase was obtained.

An approximation between angles 34 and 37° (Figure 1b) shows that the position of the peak located in the plane (002) at 34.4° and (101) at 36.2°, shifts up to 0.05° towards larger angle values with the concomitant use of the MDEL and the Co^{2+} doping in the ZnO lattice. Furthermore, simply using the lamp (Zn_MDEL) also makes the peaks shift, but with less intensity compared to the ZnCo_MDEL sample. The literature[45] reports that doping materials can alter the lattice characteristics of host materials due to the variation in atomic radii. As the basic structure of ZnO particles remained unchanged and they retained their original hexagonal structure, this indicates that Co^{2+} may have entered the lattice replacing Zn^{2+} ions and not in the empty spaces. This occurs because cobalt replaces zinc without generating lattice deformation as they have similar ionic radius (0.072 nm for Co^{2+}, 0.074 nm for Zn^{2+}).[18] Additionally, the formation and deformation of the lattice are strongly influenced by the incidence of UV-Vis radiation.

The results obtained by Rietveld refinement are displayed in Figures 1c-1f and Table 1. The fitting parameters (Rw) indicated good agreement between the calculated and observed XRD patterns for all samples. The sharp diffraction peaks of the crystals indicate a high degree of crystallinity. However, from microstrain data, it can be inferred that crystallinity of the samples varies depending on the synthesis parameters. This indicates that both the addition of Co^{2+} and the use of MDEL strongly influence the properties of the samples. A reduction in microstrain can be observed, which can be attributed to the use of MDEL and Co^{2+}, parameters that cause a reorganization of the network and the formation of particles with varying densities of structural defects, residual stresses, and lattice distortions.[16,49]

The morphology of the samples was analyzed using SEM and HR-TEM. The SEM morphologies of pure and cobalt-modified ZnO synthesized with and without MDEL are shown in Figures S3a and S3b (low and high magnification, respectively, SI section). The images show that the majority are formed of hexagonal ZnO rods with a pencil-shaped tip structure. The nanostructure features a thin hexagonal prismatic base, with radial sizes ranging between 50 and 86 nm. It is possible to observe a wide variation in the length and thickness of the base. Another observation is the formation of ZnO nanorods that have not self-assembled and remain in the form of irregular hexagonal particles. Furthermore, the formation of

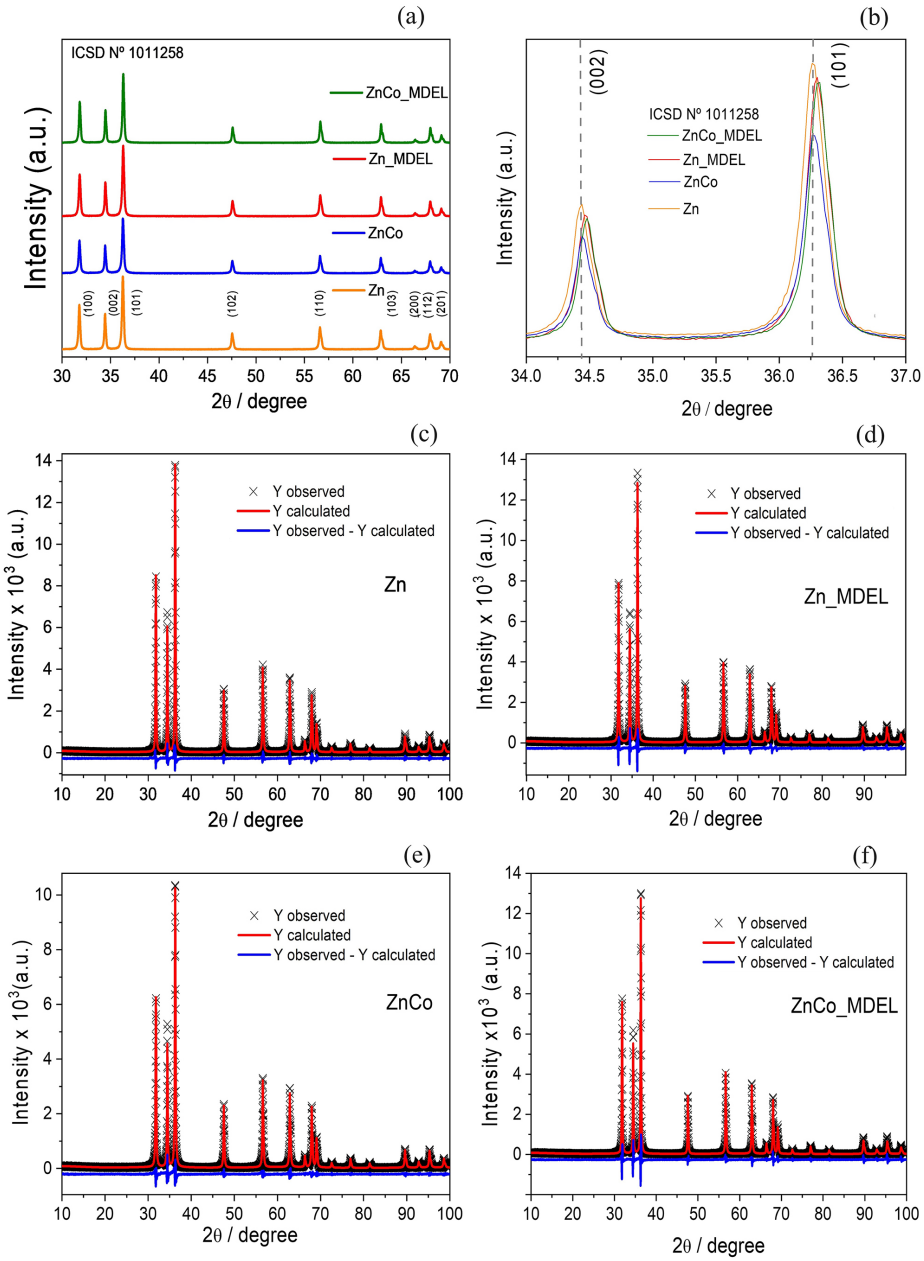

Figure 1. X-ray pattern of the pure and Co-doped ZnO samples (a), approximation of the region at 34 to 36° (b) and results of the diffraction peaks individually refined by the Rietveld technique (c-f).

Table 1. Lattice parameters obtained from Rietveld refinements of ZnO powders, bandgap energy (E_g) and radial size of the nanostructures 3D ZnO

Sample	Lattice parameters / Å		Cell volume / Å³	Crystallite size / nm	Microstrain	R factor (Rw)	Radial size / nm	E_g / eV
	a = b	c						
Zn	3.25088(5)	5.20770(7)	47.6626(9)	83.7	1004.1.9	11.7	82.8 ± 17.3	3.26
Zn_MDEL	3.24896(6)	5.20497(7)	47.5815(10)	75.3	836.5	12.3	76.8 ± 16.4	3.30
ZnCo	3.25025(6)	5.20644(7)	47.6327(10)	67.0	836.7	11.8	86.6 ± 21.6	3.29
ZnCo_MDEL	3.248008(0)	5.20352(0)	47.5400(0)	87.3	844.6	14.2	84.6 ± 16.3	3.29

E_g: band gap energy; MDEL: microwave discharge electrodeless cadmium lamp.

agglomerated structures containing rods with dimensions smaller than 10 nm is observed.

The mass percentages of each element were 75% (Zn) and 25% (O) for Zn, 79% (Zn) and 21% (O) for Zn_MDEL,

8% (Zn), 11% (O) and 1% (Co) for ZnCo and 68% (Zn), 31% (O) and 0.6% (Co) for ZnCo_MDEL (Figure S4, SI section). The doped samples were confirmed to contain Co, although the actual values found were lower than the theoretical value (< 3%). This result shows that the access of the electron beam to detect Co in the structure does not reach deep enough, for obtain a more intense signal of Co emission. Figure S5 (SI section) shows the color of each powder, and the samples modified with Co are clearly green due to the presence of the metal.

The TEM images of ZnO displayed in the inserts of Figure 2 confirm the predominant formation of hexafaceted particles larger than 50 nm, with pencil-like morphologies, and particles smaller than 10 nm, also with hexagonal faces. The spacing between diffraction spots, showed in Figures 2b, is developed along the major axis of the nanorods, resulting in values of 0.295, 0.272, 0.252, 0.232, and 0.167 nm, which correspond to the (100), (100), (101), (100) and (110) planes, respectively, confirming that the nanoparticles are oriented in the c-direction.[48] According to the results of XRD pattern and HR-TEM images, we believed that the Co ions were well incorporated into the crystal lattice of ZnO.

The histograms for calculating average particle size are shown in Figures 2c. An average radial size of ca. 85 nm

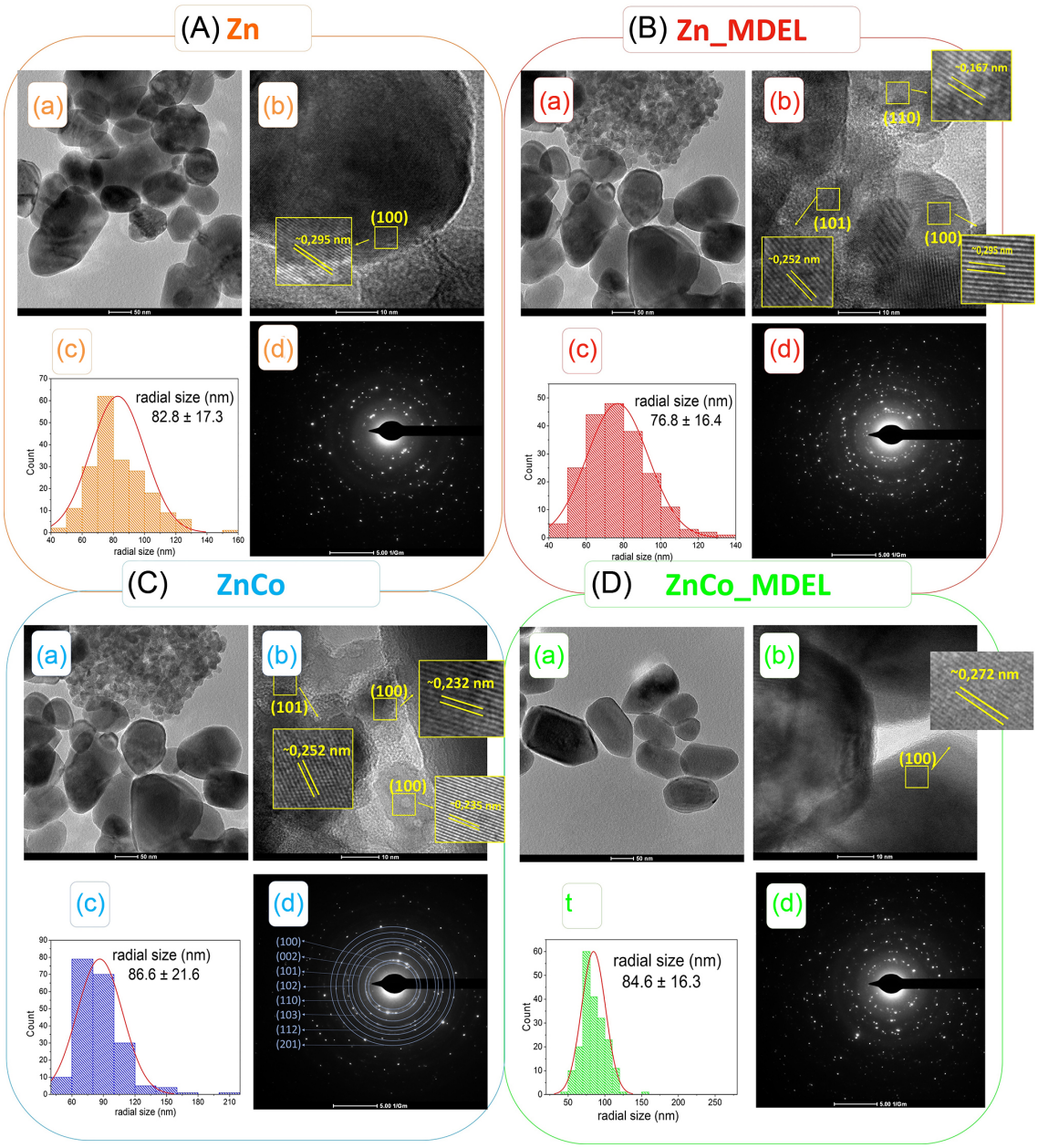

Figure 2. (A) Zn; (B) Zn_MDEL; (C) ZnCo; (D) ZNCo_MDEL. (a) TEM images of the ZnO NPs, (b) HRTEM lattice image, inset shows the d-spacing of the crystal plane, (c) histogram for calculating average particle size, and (d) SAED pattern of the ZnO sample.

can be found for the synthesized samples, which is in accordance with the crystallite size measurements obtained from the Rietveld refinement measurements presented in Table 1. The SAED pattern is shown in Figures 2d, where the characteristic diffraction rings of the ZnO hexagonal lattice can be recognized, demonstrating the crystallinity of the ZnO. Here, we can observe that the Co-doped ZnO samples present more defined diffraction rings in the SAED pattern, followed by the samples sited under the MDEL lamp. These results indicate that Co-doping causes a rearrangement in the ZnO crystal structure, increasing its organization and decreasing the density of defects in the crystal lattice. The MDEL lamp also reduces the density of sample defects, but with less intensity. This behavior affects the catalytic properties of ZnO, changing the materials characteristics.

Figure 3a shows the diffuse reflectance spectrum of the pure and cobalt-modified 3D ZnO samples. Considering the highest energies as the starting point of the scan, the first electronic transition is confirmed at approximately 370 nm for all materials, a behavior characteristic of pure ZnO.[13,14] Shifting towards lower energies, the cobalt-modified samples show additional peaks at 516, 572 and 630 nm, while the pure samples reach their maximum reflectance. The additional peaks correspond to sp-d electronic transitions between 3D ZnO and the 3d energy level of Co^{2+} successfully inserted into the 3D ZnO structure as a substitutional dopant.[50]

The bandgap energies (E_g) were ca. 3.3 eV for all materials (Figure 3b), however, the additional energy levels created by the insertion of Co^{2+} were responsible for absorbing low-energy light situated in the visible region for ZnCo and ZnCo_MDEL. As the main electronic transition occurs at 3.3 eV, these additional energy levels can act as traps for photoexcited electrons. If these trapped electrons are successfully transferred to the conduction band, the photocatalytic property of the material is optimized, otherwise the structures produced can be excellent sources of photoluminescent emission due to internal recombination processes.[19,49] Thus, the photocatalytic activity of the materials is expected under UV light irradiation.

Figure 3c presents the Mott-Schottky analysis, the positive slope observed reinforces the n-type nature of the samples. Through linear range extrapolation, the determined average E_{FB} values were 0.124, 0.131, 0.106, and 0.117 V *vs.* RHE for Zn, Zn_MDEL, ZnCo, and ZnCo_MDEL, respectively. The position of E_{fb} presents a large distribution in the literature,[51,52] and many factors contribute to this displacement such as the number of charge donors (N_D / m^{-3}). N_D was extracted from the Mott-Schottky equation being 2.41×10^{18} (Zn), 2.62×10^{18} (Zn_MDEL),

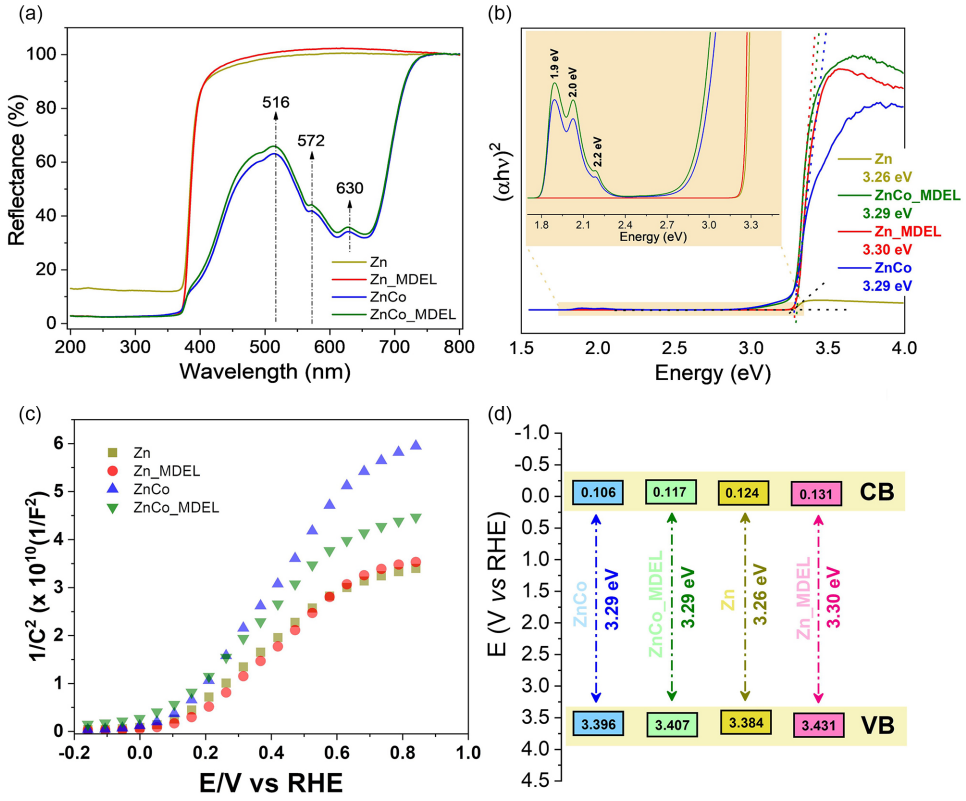

Figure 3. DRS spectra (a), Tauc plot (b), Mott-Schottky plot (c) and band structure obtained of the ZnO samples (d).

1.64×10^{18} (ZnCo), and 1.79×10^{18} (ZnCo_MDEL). These results suggest an increased number density (N_D) in two scenarios: (*i*) in samples synthesized assisted with MDEL compared to those exclusively synthesized by MHM, and (*ii*) in undoped materials compared to Co-doped samples. The introduction of cobalt may lead to a reduction in charge donors, possibly associated with the formation of deep defects.[53,54] Specifically, the substitution of Zn^{2+} by Co^{2+} in the crystal lattice introduces energy levels intermediary to the valence and conduction bands, which can impact the photocatalytic activity.

Considering the E_{fb} as approximately the edge of the conduction band (CB_{edge}) for n-type semiconductors, we were able to estimate the edge of the valence band (VB_{edge}) as well, which is presented in the Table 2 and the band structure in Figure 3d. The band energy of both samples possesses enough energy to oxidize water or dissolved oxygen, generating ROS that can be useful in further photocatalytic oxidation assays,[55] once that efficient formation of hydroxyl radicals can be achieved when the flow of electrons between the VB and CB occurs continuously.

Table 2. Parameters obtained from Mott-Schottky analysis of ZnO samples

Sample	E_{fb} (*vs.* RHE) / V	VB_{edge} (*vs.* RHE) / V	N_D / (10^{18} m^{-3})
Zn	0.124	3.384	2.41
Zn_MDEL	0.131	3.431	2.62
ZnCo	0.106	3.396	1.64
ZnCo_MDEL	0.117	3.407	1.79

RHE: reversible hydrogen electrode; E_{FB}: flat band potential; VB_{edge}: edge of the valence band; N_D: number density; MDEL: microwave discharge electrodeless cadmium lamp.

The number of charge donors is an electrochemical parameter that is directly related to catalytic processes based on the flow of electrons between VB and CB. Therefore, a 2^2 full factorial design was carried out to ascertain the influence of the variable use of UV-Vis radiation (MDEL) and the addition of cobalt on these properties. Since the unreplicated nature of the dataset, the Lenth method was employed to assess the statistical significance of effect estimates.[56] The pseudo standard error (PSE) of the Lenth method, grounded in the notion of sparse effects, was utilized to establish the statistical critical values, enabling a robust evaluation of the effects in the absence of replication. The Pareto chart (Figure 4) is a graphical representation of the significance of the studied variables and their interactions in the generation of charge donors. The incorporation of cobalt (effect B) was identified as the most relevant factor affecting the number of donors, with a contribution of 80% to the response. As observed, the higher number of charge donors is linked to the lower level of this factor; thus, the addition of cobalt produces samples with a lower quantity of charge donors. The presence of MDEL (effect A) and the combined effect (effect AB) showed relatively non-significant effects and presented a minor contribution, accounting for less than 18 and 2% of the response, respectively. The literature shows that Co^{2+} can induce shallow or deep defects in the semiconductor structure which act as intermediate levels for the moving charge donors. Shallow defects optimize charge transfer to the CB, while deep defects can trap these donors and inhibit the flow between the VB and CB, resulting in recombination.[54]

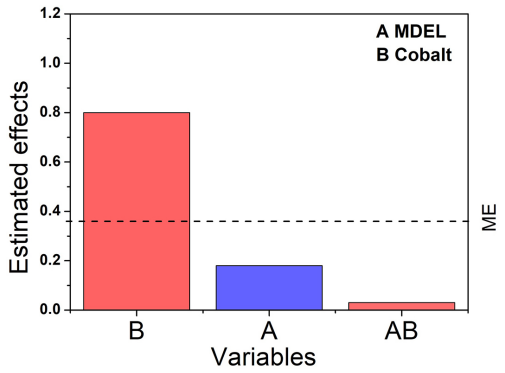

Figure 4. Pareto chart for the generation of charge donors. The red color represents a negative effect, and the blue color represents a positive effect.

Other hypotheses that may explain the effects of cobalt and MDEL on the response are the photochemical reactions that may take place during the crystallization of ZnO. As shown in Figure S2 (SI section), the MDEL emits light with λ ca. 195 nm and sufficient energy to trigger the reactions described by equations 2 to 5. As the effect of MDEL on the response is less pronounced compared to cobalt, the reaction mechanisms triggered by MDEL can be correlated to the mechanisms of to the mechanisms of Co^{2+}/Co^{3+} species formation.

$$H_2O + MDEL\ (\lambda \sim 195\ nm) \rightarrow {}^{\bullet}OH + H^+ + e^-_{(aq)} \quad (2)$$

$${}^{\bullet}OH + Co^{2+} \rightarrow Co^{3+} + OH^- \quad (3)$$

$$e^-_{(aq)} + Co^{3+} \rightarrow Co^{2+} \quad (4)$$

$$Zn^{2+} + 2OH^- \rightarrow ZnO\ (nuclei) + H_2O \quad (5)$$

These different oxidation states of cobalt that can be present in the ZnO structure produce oxygen vacancies ($V_{Ö}$) in search of charge neutrality in the crystal structure. As $V_{Ö}$ are listed as active sites for charge mobility, the photocatalytic activity of the semiconductor tends to be optimized.

Catalytic assays

eCO$_2$RR

Electrochemical experiments were conducted to investigate (*i*) the impact of incorporation of cobalt on the ZnO and (*ii*) the influence of MDEL during the synthesis process for CO_2 reduction reaction. Figure 5 illustrates the correlation between various applied potential values and the faradaic efficiency of CO generation, which is the main gaseous outcome in the conversion of CO_2 using Zn-based materials.[57] The examination of the faradaic efficiency of the CO_2 to CO conversion process, utilizing samples generated through microwave synthesis, with and without the presence of the MDEL, demonstrates that the performance of Zn > ZnMDEL > ZnCo_MDEL > ZnCo.

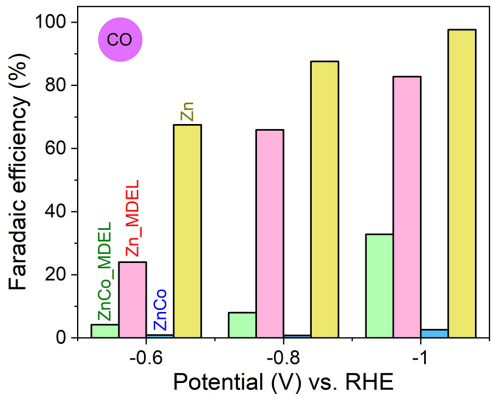

Figure 5. Faradaic efficiency (%) for the electrocatalytic conversion of CO_2 to CO.

In the Zn sample, the positive potential of the CB is slightly lower than that seen for the Zn_MDEL sample, as shown in Table 2. Even though the Zn_MDEL sample has the highest number of charge donors, for the reactions at –0.6 V *vs*. RHE, the migration of charges to the CB is not effective due to the position of the band at a more positive potential. At a potential of –0.6 V *vs*. RHE, the sample Zn_MDEL exhibited a faradaic efficiency of 24%, whereas the sample Zn had an efficiency of 68%. Nevertheless, this difference diminishes as the applied potential rises, reaching 83 and 97%, respectively, at a potential of –1.0 V *vs*. RHE.

Upon examining the impact of cobalt on the transformation of CO_2 into CO through the suggested synthesis techniques, it is evident that the faradaic efficiency for CO at –0.6V *vs*. RHE is 4.2 and 1% for the samples with and without a MDEL, respectively. Nevertheless, as the applied potential rises, as previously mentioned, the conversion efficiency from CO_2 to CO becomes more noticeable for ZnCo_MDEL. This inefficiency in CO_2 conversion due to the presence of Co^{2+} is explained by the sharp drop in charge donors (Table 2), which can be trapped in intermediate levels formed by deep defects in the structure. However, the presence of MDEL seems to alter the nature of these defects and contribute to the flow of electrons at higher reaction potentials. The faradaic efficiency of the sample synthesized in the presence of the MDEL is only 2.6%, but the sample under –1.0 V *vs*. RHE achieves a faradaic efficiency of up to 33%. Similar to the cobalt-free sample, the microwave approach assisted by the cadmium lamp, exhibits superior efficacy at elevated applied potentials, indicating the ability of the material to function optimally at elevated current densities, which is a key objective for the widespread conversion of CO_2.[58]

The excellent results of CO_2 reduction and selective conversion to CO confirm that the materials obtained in this study are an alternative to be future explored in pilot eCO$_2$RR systems. The high faradaic efficiency implies that the CO conversion reactions are environmentally friendly, energetically favorable, and industrially interesting, since CO is a precursor in numerous processes in the chemical and pharmaceutical industries.

Photocatalytic degradation

Monitoring analysis

Prior to the photodegradation assays, the methods for monitoring OFX and SRTL using EEM in tandem with PARAFAC were developed. The EEM of a surface water sample fortified with 240 μg L^{-1} of OFX showed a peak centered at λ_{exc} = 288 nm and λ_{em} = 459 nm (Figure S6a, SI section). Sodium diclofenac (200 μg L^{-1}) was added to the solution as a concomitant in addition to the organic matter naturally present in the water sample. The peak centered at λ_{exc} = 287 nm and λ_{em} = 365 nm was attributed to DCF; however, its intensity was lower than of OFX. Applying PARAFAC to decompose the EEM spectra, five components were recovered in the mixture, with component 1 (C1) attributed to OFX, component 3 (C3) attributed to DCF, and components C2, C4, and C5 were classified as unknown, related to the compounds present in the sample matrix. The calibration curve for OFX was obtained (Figure S6a), with a good linear fit (R^2 = 0.996), LOD = 5.2 μg L^{-1}, and LOQ = 15.9 μg L^{-1}. The SRTL, on the other hand, exhibits a peak centered at λ_{exc} = 262 nm and λ_{em} = 285 nm, as shown in Figure S6b. After the decomposition of the EEM data, 3 components were recovered, with 2 also classified as unknown. The calibration curve for SRTL obtained (Figure S6b) showed a good linear fit (R^2 = 0.992), LOD = 63.6 μg L^{-1}, and LOQ = 192.8 μg L^{-1}.

Photocatalysis screening

The number of charge donors in a semiconductor is a relevant parameter for photocatalytic applications, since the mobility of these species when excited by light results in photoactivity. In this way, we chose between the catalysts, a pure and a Co-doped that contained the largest amount of donors (Zn_MDEL and ZnCo_MDEL samples), which also showed electrocatalytic activity in CO_2RR. Then, the photocatalysts were exposed to two degradation environments: one comprising a mixture of STR + FLX, and the other of OFX + DCF. The aim was to evaluate the condition with the highest removal efficiency. Therefore, we computed the proportional impact of each factor on the percentage of removal, coupled with their cumulative total, to assess the efficacy of strategies wielding substantial influence (Figure 6a). The choice of catalyst (effect A), drug mixture (effect B), and their interaction (effect AB) were recognized as significant factors influencing the removal efficiency.

The normal probability plot depicted in Figure 6b shows that the negative value of effect A means a decrease in removal efficiency with the change from Zn_MDEL to ZnCo_MDEL. In other words, a higher percentage of removal is obtained with the utilization of the Zn_MDEL catalyst. This result is explained by the number of charges donors present in this sample, which was 36% higher than that found in ZnCo_MDEL (Table 2). The variable B has also shown a substantial effect on the system, and its positive value means that a higher removal efficiency was obtained in the photodegradation of the mixture OFX + DCF. The lowest removal rates observed for the SRTL + FLX mixture are due to the lower verified polar surface area (PSA) for these molecules APS = 12 Å^2 (SRTL) and APS = 21.3 Å^2 (FLX) compared to the OFX + DCF mixture, which have values APS = 73.3 Å^2 (OFX) and APS = 49.3 Å^2 (DCF) according to the National Center for Biotechnology Information.[59]

As the 3D ZnO nanostructures have semi-polar and nonpolar facets available, the interaction of SRTL + FLX with the photocatalyst is favored over the OFX + DCF mixture. This interaction of OFX + DCF with the photocatalyst is even lower at the reaction pH (ca. 6.5), since pK_a = 5.97 (OFX), pK_a = 4.2 (DCF), pK_a = 9.16 (SRTL) and pK_a = 9 (FLX).[59] Because they are protonated at the reaction pH, SRTL + FLX can approach the catalyst surface due to the $-O_2^-$ sites generally exposed and block photocatalytic sites responsible for ROS production. On the other hand, OFX + DCF in its deprotonated form undergoes repulsion and has little interaction with the photocatalyst, its removal being conditioned to the formation of ROS and direct degradation within the aqueous solution. Furthermore, the relevance of the cross-effect AB is evident, underscoring its importance in understanding the system dynamics. Interestingly, the second most significant variable is a second-order one: the interaction between catalyst and drug. This implies that the interplay between catalyst and drug induces more substantial changes in removal than drug alone. While first-order variables are typically more influential, this observation supports that the interaction between the catalyst and the environment significantly alters removal efficiency. As the OFX + DCF mixture is more susceptible to oxidation by ROS because they are more available in the solution, this was selected to kinetic assays in Zn_MDEL and ZnCo_MDEL presence.

Kinetic assays

Figure 7 shows the 3D spectrum of the original solution (Figure 7a) and after photocatalytic degradation at 15 min (Figure 7b) and 30 min (Figure 7c) using Zn_MDEL under UV-C light irradiation.

Removal by adsorption was 40% for both materials. As the pH of the reaction (6.5) is close to the pK_a value = 5.9 of OFX, deprotonated and neutral species are expected on solution, and the latter can be adsorbed on the catalyst surface. When UV-C light was activated, the decrease in the PL intensity of OFX was related to a photocatalytic

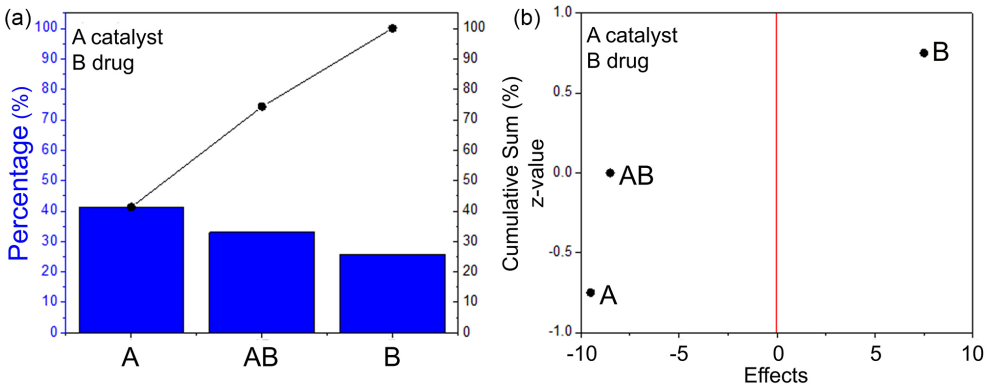

Figure 6. Percentage of each effect and cumulative sum on the pollutant removal (a) and the probability graph of effects (b).

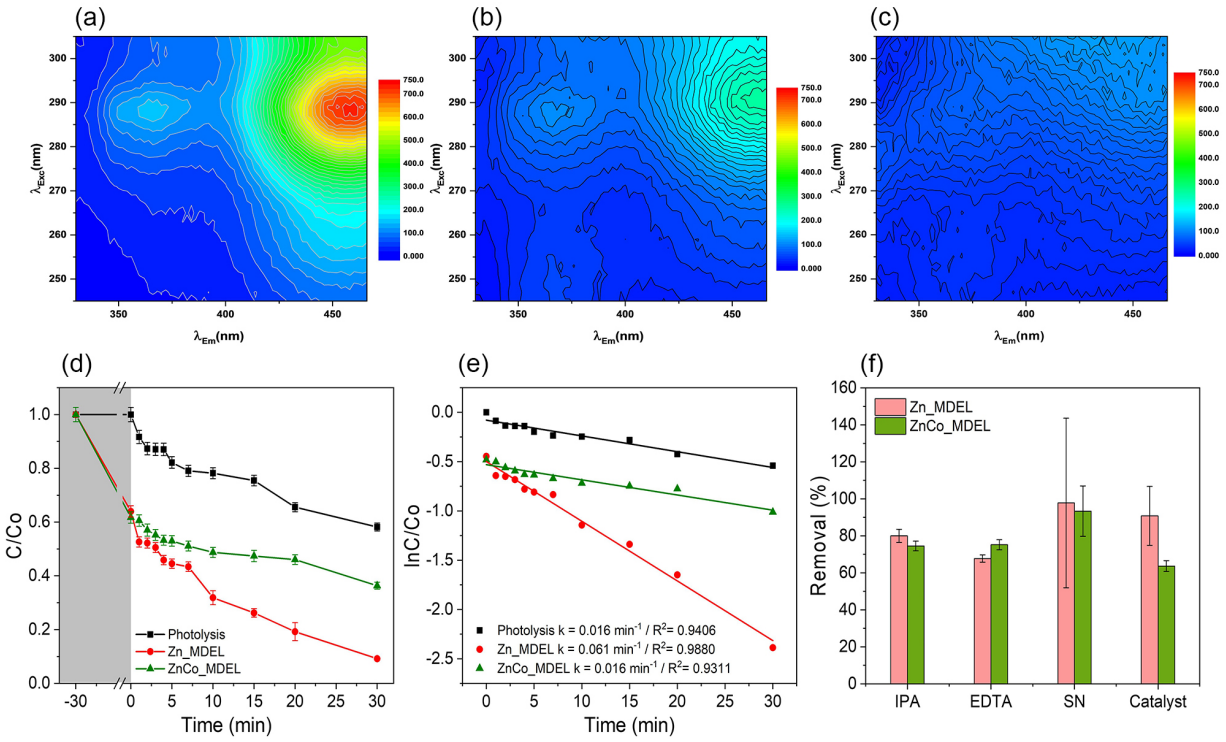

Figure 7. EEM spectra of the original OFX solutions (a), degraded in 15 min (b) and 30 min (c) under UV-C light in the presence of the Zn_MDEL catalyst. Degradation of OFX over time (d), kinetic constant (e) and study with scavengers under UV-C light at 30 min (f).

degradation of 91% within 30 min. Figure 7d shows the C/Co ratio of OFX over irradiation time for photolysis and photocatalysis using Zn_MDEL or ZnCo_MDEL. Comparatively, the removal from the photocatalytic process was superior to photolysis, with the Zn_MDEL-mediated process standing out, which we have already highlighted as having the highest number of charges donors. The pseudo-first order kinetic constants (k / min^{-1}) and linear correlation coefficients (R2) were k × 10^{-2} = 1.6 min^{-1}, R^2 = 0.9406 for photolysis; k × 10^{-2} = 6.1 min^{-1}, R^2 = 0.9880 for Zn_MDEL and k × 10^{-2} = 1.6 min^{-1}, R2 = 0.9311 for ZnCo_MDEL.

The degradation mechanism was investigated using different scavengers for the reactive oxygen species produced in the photocatalytic process (Figure 7f). The degradation of OFX is slightly inhibited in the presence of IPA and EDTA, showing that hydroxyl radicals and holes, respectively, are the most important photocatalytic mechanisms for Zn_MDEL. For ZnCo_MDEL, none of the scavengers showed relevant inhibition, showing that the reactive species linked to the scavengers used were not significant. The experiments with AAS as an $O_2^{\bullet-}$ scavenger showed interference in the quantification of OFX by the EEM method, and therefore the production of $O_2^{\bullet-}$ by the photolytic process cannot be ruled out. These results explain the correspondence of the k values for photolysis and ZnCo_MDEL photocatalysis, as well as the fourfold increase in the k value for Zn_MDEL compared to photolysis and ZnCo_MDEL. Evidence of the formation of hydroxyl radicals in the presence of Zn_MDEL or ZnCo_MDEL using the coumarin probe assay is shown in Figure S7 (SI section). Scheme 1 shows the conversion of coumarin (COU) into 7HC, the latter being a product resulting from the hydroxylation of COU and showing an excitation and emission peak at 330 and 460 nm, respectively.

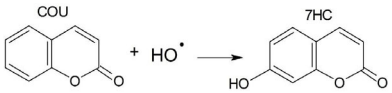

Scheme 1. Conversion of coumarin into 7HC.

Figure S7a (SI section) confirms the formation of 7HC in the presence of Zn_MDEL, while the low PL intensity for ZnCo_MDEL (Figure S7b) confirms that the formation of 7HC was not significant for this system. Using a calibration curve obtained from PARAFAC, the concentration of 7HC was calculated. This value was used to calculate the hydroxyl radical concentration using the method proposed by Nagarajan *et al.*[46] The production of radicals was 0.18 or 0.06 µmol L^{-1} h^{-1} for Zn_MDEL or ZnCo_MDEL, respectively. Here, radical production was three times higher for Zn_MDEL compared to ZnCo_MDEL, which is compatible with the analyses of physicochemical characterization of material the better performance in

OFX degradation. Therefore, the set of equations 6 to 10 summarizes the photocatalytic mechanism of Zn_MDEL to promote the degradation of OFX.

$$Zn\_MDEL + h\nu \rightarrow h^{+}(VB) + e^{-}(CB) \quad (6)$$
$$h^{+}(VB) + H_2O \rightarrow {}^{\bullet}OH + H^{+} \quad (7)$$
$${}^{\bullet}OH + OFX \rightarrow byproducts \quad (8)$$
$$e\text{-}(CB) + O_2 \rightarrow O_2^{\bullet-} \quad (9)$$
$$O_2^{\bullet-} + OFX \rightarrow byproducts \quad (10)$$

The results of the photocatalytic degradation of OFX using real matrices confirm that ZnO-based materials are promising candidates for further studies in flow systems in wastewater treatment plants. For this purpose, it is necessary to attach the ZnO-based nanomaterials to substrates for use in large-volume photocatalytic reactors. As the materials are synthesized in the presence of EG, which is widely used to attach nanostructures to substrates, the challenges of this step can be overcome. Thus, our results offer an alternative for developing efficient processes to degrade organic pollutants in environmental matrices.

Challenges and opportunities

The method of synthesizing nanomaterials presented in this study shows many opportunities for future research and advancement in the field. Among the topics to be explored are: development of computational methods that can show the relationship between light and the crystal structures produced; how different metal precursors can optimize light absorption in the crystallization stage; how light intensity can influence the formation of specific defects in materials; the ability of light to produce metal ions with different oxidation states in the ceramic structures, as well as the opportunity to develop different light sources (MDEL) with different emission spectra. However, the biggest challenges for progress in this field are related to the need to build specific microwave reactors for synthesizing nanomaterials and new MDELs for operating at low microwave powers. These new reactors need to be designed to: produce larger quantities of materials; allow working with a wide range of microwave power; withstand high temperatures, time and pressures due to the application of constant microwave power; feature integrated devices that enable precise monitoring of pressure, temperature and the electromagnetic spectrum emitted by the light source (MDEL).

Conclusions

Using a little-explored approach to produce nanomaterials in which the synergy between microwave, ultraviolet and visible radiation is applied in synthesis processes, nanostructures of pure ZnO and cobalt-doped ZnO were obtained. The structural characterization showed that Co^{2+} is inserted into the ZnO lattice and promotes a peak shift at positions 34 and 37° (2θ), an observation also confirmed when MDEL is used. The effect of the presence of Co^{2+} on the numerous charge donors was confirmed by the experimental design analysis, and the diffuse reflectance data showed the presence of intermediate energy levels in the absorption regions at 516, 572 and 630 nm for the doped samples. All materials were characterized as n-type semiconductors by positioning the BC at positive potentials. The Mott-Schottky analyses revealed that the number of charge donors increased in the following order: Zn_MDEL > Zn > ZnCo_MDEL > ZnCo. This suggests that MDEL produced materials with a higher number of charge donors for samples with the same chemical composition. When applied to the CO_2RR reaction, the pure samples stood out with EF = 97%, while the ZnCo_MDEL sample showed improvements in the conversion of CO_2 to CO under higher potential energy conditions. The degradation studies of the emerging contaminants achieved up to 91% removal in 30 min of irradiation, and the degradation mechanisms through the production of hydroxyl radicals were confirmed. Here, the nature of the chemical composition of the degradation solutions was a relevant aspect in the efficiency of photocatalysis, and the interaction with the catalyst was also considered. Thus, this study has gathered important information on the use of a new synthesis method to produce nanostructures with photocatalytic properties for environmental remediation.

Supplementary Information

Supplementary data (synthesis system, microwave power and temperature profile, FEG-MEV, EDS-MEV, picture of powders, EEM spectra, DoE table, physicochemical characterization of surface water) are available free of charge at http://jbcs.sbq.org.br as PDF file.

Acknowledgments

This work was financially supported by Coordenação de Aperfeiçoamento de Pessoal de Nível Superior (CAPES) - Finance Code 001, Fundação de Amparo à Pesquisa do Estado de São Paulo (grants: 2013/07296-2, 2019/26860-2, 2021/12394-0, 2022/05254-0, 2022/06219-3, 2022/10255-5, 2023/07525-3, 2023/11554-9), Conselho Nacional de Desenvolvimento Científico e Tecnológico

(CNPq) grants: 383432/2023-5, DTI-A is gratefully acknowledged.

Author Contributions

Eryka T. D. Nobrega was responsible for experimental design, writing - original draft and methodology; Kelvin C. de Araújo for methods and experiments (EEM-PARAFAC analysis); Ailton J. Moreira for developed the photocatalysis experiments, writing and review; Regiane C. de Oliveira for structural properties and Rietveld refinement analysis; Gelson T. S. T. da Silva for methodology, analysis, writing (CO_2RR); Sirlon F. Blaskievicz and Leandro L. Soares for methodology, electrochemical data analysis, writing (electrochemical properties); Sherlan G. Lemos for data analysis, methodology, writing - editing (EEM-PARAFAC and Experimental Design); Lucia H. Mascaro for writing, review and editing (electrochemical properties); Ernesto C. Pereira for supervision, resources, writing - review and editing.

References

1. MacWan, D. P.; Dave, P. N.; Chaturvedi, S.; *J. Mater. Sci.* **2011**, *46*, 3669. [Crossref]
2. Marques, G. N.; Moreira, A. J.; Nóbrega, E. T. D.; Braga, S.; Argentin, M. N.; da Cunha Camargo, I. L. B.; Azevedo, E.; Pereira, E. C.; Bernardi, M. I. B.; Mascaro, L. H.; *J. Environ. Chem. Eng.* **2024**, *12*, 111870. [Crossref]
3. Malafatti, J. O. D.; Moreira, A. J.; Paris, E. C.; Cardenas Flechas, L. J.; Pereira, O. A. P.; Rincón Joya, M.; *Catalysts* **2022**, *12*, 1199. [Crossref]
4. Wang, J.; Ma, J.; Zhang, Q.; Chen, Y.; Hong, L.; Wang, B.; Chen, J.; Jing, H.; *Appl. Catal., B* **2021**, *285*, 119781. [Crossref]
5. de Oliveira, C.; Renda, C. G.; Moreira, A. J.; Pereira, O. A. P.; Pereira, E. C.; Freschi, G. P. G.; Bertholdo, R.; *Environ. Res.* **2023**, *219*, 115054. [Crossref]
6. Paris, E. C.; Malafatti, J. O. D.; Moreira, A. J.; Santos, L. C.; Sciena, C. R.; Zenatti, A.; Escote, M. T.; Mastelaro, V. R.; Joya, M. R.; *Environ. Sci. Pollut. Res.* **2022**, *29*, 41505. [Crossref]
7. Pinheiro, B. S.; Moreira, A. J.; Gimenes, L. L. S.; Freschi, C. D.; Freschi, G. P. G.; *Environ. Monit. Assess.* **2020**, *192*, 331. [Crossref]
8. Pinheiro, B. S.; Gimenes, L. L.; Moreira, A. J.; de Araújo, A. F.; Freschi, C. D.; Freschi, G. P. G.; *J. Environ. Sci. Health, Part A: Toxic/Hazard. Subst. Environ. Eng.* **2017**, *52*, 1089. [Crossref]
9. Mazivila, S. J.; Ricardo, I. A.; Leitão, J. M. M.; da Silva, J. C. G. E.; *Trends Environ. Anal. Chem.* **2019**, *24*, e00072. [Crossref]
10. Ansari, S. A.; Ansari, S. G.; Foaud, H.; Cho, M. H.; *New J. Chem.* **2017**, *41*, 9314. [Crossref]
11. Ansari, S. A.; Parveen, N.; Alsulaim, G. M.; Ansari, A. A.; Alsharif, S. A.; Alnahdi, K. M.; Alali, H. A.; Reddy, V. R. M.; *Surf. Interfaces* **2023**, *40*, 103078. [Crossref]
12. Ansari, S. A.; *Ceram. Int.* **2023**, *49*, 17746. [Crossref]
13. Silva, T. E. M.; Moreira, A. J.; Nobrega, E. T. D.; Alencar, R. G.; Rabello, P. T.; Blaskievicz, S. F.; Marques, G. N.; Mascaro, L. H.; Paris, E. C.; Lemos, S. G.; Pereira, E. C.; Freschi, G. P. G.; *Chem. Eng. J.* **2023**, *475*, 146235. [Crossref]
14. Šutka, A.; Käämbre, T.; Pärna, R.; Juhnevica, I.; Maiorov, M.; Joost, U.; Kisand, V.; *Solid State Sci.* **2016**, *56*, 54. [Crossref]
15. Mylsamy, S.; Govindasamy, T.; Subramanian, B.; *J. Environ. Chem. Eng.* **2024**, *12*, 111700. [Crossref]
16. Karpyna, V.; Myroniuk, L.; Myroniuk, D.; Bykov, O.; Olifan, O.; Kolomys, O.; Strelchuk, V.; Bugaiova, M.; Kovalchuk, I.; Ievtushenko, A.; *Catal. Lett.* **2023**. [Crossref]
17. Khalid, A.; Ahmad, P.; Alharthi, A. I.; Muhammad, S.; Khandaker, M. U.; Faruque, M. R. I.; Khan, A.; Din, I. U.; Alotaibi, M. A.; Alzimami, K.; Alfuraih, A. A.; Bradley, D. A.; *Materials* **2021**, *14*, 3223. [Crossref]
18. Dhiman, M.; Tripathi, M.; Singhal, S.; *Mater. Chem. Phys.* **2017**, *202*, 40. [Crossref]
19. Bergoug, S.; Achouri, A.; Benhamida, S.; Manseri, A.; Belkhalfa, H.; Landolsi, Z.; Taabouche, A.; Naitbouda, A.; Chelouche, A.; *Phys. B* **2024**, *674*, 415586. [Crossref]
20. Kumar, P.; Kumar, R.; Singh, R. In *Encyclopedia of Materials: Plastics and Polymers*, vol. 1; Hashmi, M. S. J., ed.; Elsevier, 2022, p. 632. [Crossref]
21. Moreira, A. J.; Coelho, D.; Dias, J. A.; Mascaro, L. H.; Freschi, G. P. G.; Mastelaro, V. R.; Pereira, E. C.; *J. Alloys Compd.* **2022**, *905*, 164217. [Crossref]
22. Kumar, A.; Kuang, Y.; Liang, Z.; Sun, X.; *Mater. Today Nano* **2020**, *11*, 100076. [Crossref]
23. Mazzolini, P.; Russo, V.; Casari, C. S.; Hitosugi, T.; Nakao, S.; Hasegawa, T.; Li Bassi, A.; *J. Phys. Chem. C* **2016**, *120*, 18878. [Crossref]
24. Humayun, M.; Raziq, F.; Khan, A.; Luo, W.; *Green Chem. Lett. Rev.* **2018**, *11*, 86. [Crossref]
25. Wang, B.; Chen, W.; Song, Y.; Li, G.; Wei, W.; Fang, J.; Sun, Y.; *Catal. Today* **2018**, *311*, 23. [Crossref]
26. Xu, Q.; Jin, Y.; Sun, T.; Zheng, T.; Zhang, P.; Han, Y.; Wang, Y.; Li, T.; Qi, D.; Xu, L.; Wang, D.; Jiang, J.; *Chem. Eng. J.* **2024**, *479*, 147837. [Crossref]
27. Mustapha, U.; Nnadiekwe, C. C.; Alhaboudal, M. A.; Yunusa, U.; Abdullahi, A. H. S.; Abdulazeez, I.; Hussain, I.; Ganiyu, S. A.; Al-Saadi, A. A.; Alhooshani, K.; *J. Energy Chem.* **2023**, *85*, 198. [Crossref]
28. Gupta, S.; Fernandes, R.; Patel, R.; Spreitzer, M.; Patel, N.; *Appl. Catal., A* **2023**, *661*, 119254. [Crossref]
29. Aquatic Life Criteria for Contaminants of Emerging Concern, https://www.epa.gov/sites/default/files/2015-08/documents/white_paper_aquatic_life_criteria_for_contaminants_of_emerging_concern_part_i_general_challenges_and_recommendations_1.pdf, accessed in April 2024.

30. Kroon, F. J.; Berry, K. L. E.; Brinkman, D. L.; Kookana, R.; Leusch, F. D. L.; Melvin, S. D.; Neale, P. A.; Negri, A. P.; Puotinen, M.; Tsang, J. J.; van de Merwe, J. P.; Williams, M.; *Sci. Total Environ.* **2020**, *719*, 135140. [Crossref]
31. Moreira, A. J.; Blaskievicz, S. F.; de Assis, M.; Marques, G. N.; Menezes, W. T.; Rabello, P. T.; Rabahi, C.; Gobato, Y. G.; Freschi, G. P. G.; Mascaro, L. H.; Pereira, E. C.; *Res. Chem. Intermed.* **2024**, *50*, 297. [Crossref]
32. Khan, N. A.; López-Maldonado, E. A.; Majumder, A.; Singh, S.; Varshney, R.; López, J. R.; Méndez, P. F.; Ramamurthy, P. C.; Khan, M. A.; Khan, A. H.; Mubarak, N. M.; Amhad, W.; Shamshuddin, S. Z. M.; Aljundi, I. H.; *Chemosphere* **2023**, *344*, 140264. [Crossref]
33. Zhang, H.; Bayen, S.; Kelly, B. C.; *Sci. Total Environ.* **2015**, *523*, 219. [Crossref]
34. Akvan, N.; Azimi, G.; Parastar, H.; *Microchem. J.* **2019**, *150*, 104056. [Crossref]
35. Moreira, A. J.; Lemos, S. G.; Coelho, D.; Mascaro, L. H.; Freschi, G. P. G.; Pereira, E. C.; *Environ. Sci. Pollut. Res.* **2021**, *29*, 24010. [Crossref]
36. Araújo, K. C.; Nóbrega, E. T. D.; Moreira, A. J.; Lemos, S. G.; Fragoso, W. D.; Pereira, E. C.; *Catal. Commun.* **2023**, 106834. [Crossref]
37. Toby, B. H.; Von Dreele, R. B.; *J. Appl. Crystallogr.* **2013**, *46*, 544. [Crossref]
38. López, R.; Gómez, R.; *J. Sol-Gel Sci. Technol.* **2012**, *61*, 1. [Crossref]
39. Subudhi, S.; Paramanik, L.; Sultana, S.; Mansingh, S.; Mohapatra, P.; Parida, K.; *J. Colloid Interface Sci.* **2020**, *568*, 89. [Crossref]
40. Bro, R.; *Chemom. Intell. Lab. Syst.* **1997**, *38*, 149. [Crossref]
41. Olivieri, A. C.; Wu, H.-L.; Yu, R.-Q.; *Chemom. Intell. Lab. Syst.* **2009**, *96*, 246. [Crossref]
42. Barreto, M. C.; Braga, R. G.; Lemos, S. G.; Fragoso, W. D.; *Food Chem.* **2021**, *364*, 130407. [Crossref]
43. Lima, A. E. B.; Reis, R. Y. N.; Ribeiro, L. S.; Ribeiro, L. K.; Assis, M.; Santos, R. S.; Fernandes, C. H. M.; Cavalcante, L. S.; Longo, E.; Osajima, J. A. O.; Luz, G. E.; *J. Alloys Compd.* **2021**, *863*, 158731. [Crossref]
44. Nguyen Thi, H.-T.; Tran Thi, K.-N.; Hoang, N. B.; Tran, B. T.; Do, T. S.; Phung, C. S.; Nguyen Thi, K.-O.; *Materials* **2021**, *14*, 7741. [Crossref]
45. Moreira, A. J.; Malafatti, J. O. D.; Giraldi, T. R.; Paris, E. C.; Pereira, E. C.; de Mendonça, V. R.; Mastelaro, V. R.; Freschi, G. P. G.; *J. Environ. Chem. Eng.* **2020**, *8*, 104543. [Crossref]
46. Nagarajan, S.; Skillen, N. C.; Fina, F.; Zhang, G.; Randorn, C.; Lawton, L. A.; Irvine, J. T. S.; Robertson, P. K. J.; *J. Photochem. Photobiol., A* **2017**, *334*, 13. [Crossref]
47. Gonzalez, M.; Oliveros, E.; Worner, M.; Braun, A.; *J. Photochem. Photobiol., C* **2004**, *5*, 225. [Crossref]
48. Abrahams, S. C.; Bernstein, J. L.; *Acta Cryst. Sect. B Struct. Crystallogr. Cryst. Chem.* **1969**, *25*, 1233. [Crossref]
49. Zhao, L.-L.; Wang, J.-Y.; Wang, X. L.; Cheng, Z. X.; Wang, J.; Yin, N.; Gai, Z. G.; Jalalian, A.; Dou, S.-X.; *J. Alloys Compd.* **2015**, *628*, 303. [Crossref]
50. Gaur, L. K.; Gairola, P.; Gairola, S. P.; Mathpal, M. C.; Kumar, P.; Kumar, S.; Kushavah, D.; Agrahari, V.; Aragon, F. F. H.; Soler, M. A. G.; Swart, H. C.; *J. Alloys Compd.* **2021**, *868*, 159189. [Crossref]
51. Patel, M. Y.; Mortelliti, M. J.; Dempsey, J. L.; *Chem. Phys. Rev.* **2022**, *3*, 011303. [Crossref]
52. Hankin, A.; Bedoya-Lora, F. E.; Alexander, J. C.; Regoutz, A.; Kelsall, G. H.; *J. Mater. Chem. A* **2019**, *7*, 26162. [Crossref]
53. Jakani, M.; Campet, G.; Claverie, J.; Fichou, D.; Pouliquen, J.; Kossanyi, J.; *J. Solid State Chem.* **1985**, *56*, 269. [Crossref]
54. He, R.; Hocking, R. K.; Tsuzuki, T.; *Mater. Chem. Phys.* **2012**, *132*, 1035. [Crossref]
55. Cheeseman, S.; Christofferson, A. J.; Kariuki, R.; Cozzolino, D.; Daeneke, T.; Crawford, R. J.; Truong, V. K.; Chapman, J.; Elbourne, A.; *Adv. Sci.* **2020**, *7*, 1902913. [Crossref]
56. Lenth, R. V.; *Technometrics* **1989**, *31*, 469. [Crossref]
57. Stamatelos, I.; da Silva, G. T. S. T.; Ribeiro, C.; Shviro, M.; *ACS Appl. Energy Mater.* **2023**, *6*, 11510. [Crossref]
58. Masel, R. I.; Liu, Z.; Yang, H.; Kaczur, J. J.; Carrillo, D.; Ren, S.; Salvatore, D.; Berlinguette, C. P.; *Nat. Nanotechnol.* **2021**, *16*, 118. [Crossref]
59. NLM Literature Archive (NLM LitArch), https://www.ncbi.nlm.nih.gov/books/NBK51661/, accessed in April 2024.

Submitted: February 21, 2024
Published online: April 16, 2024